Title: Transient Water Vapor at Europa's South Pole

Authors: Lorenz Roth[1,2]*†, Joachim Saur[2]†, Kurt D. Retherford[1], Darrell F. Strobel[3,4], Paul D. Feldman[4], Melissa A. McGrath[5], Francis Nimmo[6]

Affiliations:

[1] Southwest Research Institute, San Antonio, TX, USA;

[2] Institute of Geophysics and Meteorology, University of Cologne, Germany;

[3] Department of Earth and Planetary Science, The Johns Hopkins University, Baltimore, MD, USA;

[4] Department of Physics and Astronomy, The Johns Hopkins University, Baltimore, MD, USA;

[5] NASA Marshall Space Flight Center, Huntsville, AL, USA;

[6] Department of Earth and Planetary Sciences, University of California Santa Cruz, CA, USA.

* Correspondence to: lorenz.roth@swri.edu

† These authors contributed equally to this work

Abstract: In November and December 2012 the Hubble Space Telescope (HST) imaged Europa's ultraviolet emissions in the search for vapor plume activity. We report statistically significant coincident surpluses of hydrogen Lyman-α and oxygen OI130.4 nm emissions above the southern hemisphere in December 2012. These emissions are persistently found in the same area over ~7 hours, suggesting atmospheric inhomogeneity; they are consistent with two 200 km high plumes of water vapor with line-of-sight column densities of about 10^{20} m^{-2}. Non-detection in November and in previous HST images from 1999 suggests varying plume activity that might depend on changing surface stresses based on Europa's orbital phases. The plume is present when Europa was near apocenter, and not detected close to its pericenter in agreement with tidal modeling predictions.

Main Text: Europa's exceptional surface morphology suggests the existence of a layer of liquid water under the icy crust *(1,2)*, which has been confirmed independently by magnetometer measurements *(3)*. Despite signs of active resurfacing in chaos terrains *(4)* and the existence of a subsurface ocean, current geologic activity has not been observed directly in Voyager and Galileo observations *(2,5,6)* or in any other data. Europa also possesses a tenuous atmosphere generated by sputtering and radiolysis *(7-9)* that was detected in 1995 through HST ultraviolet (UV) observations of oxygen emissions at 130.4 nm and 135.6 nm *(10,11)*. Spatially revolved images of these atmospheric emissions obtained by the HST Space Telescope Imaging Spectrograph (STIS) revealed an irregular emission pattern at the two oxygen multiplets, which originates from an inhomogeneous neutral gas abundance across the surface *(12,13)* or Europa's highly variable plasma environment, or both. An enhanced emission near 90° west longitude when Europa was near its apocenter detected by the HST Advanced Camera for Surveys (ACS) was associated with a possible existence of plumes in a region where high shear stresses are expected, but an unambiguous correlation was not possible due to low data quality *(14)*.

We report STIS spectral images of Europa's trailing/anti-Jovian hemisphere and leading hemisphere obtained in November and December 2012, respectively. Previous observations, in

1999, targeted Europa's trailing hemisphere (Table 1). The observations in 2012 were timed to coincide with the maximum variation of the Jupiter's magnetic field orientation at Europa. With this configuration, spatially inhomogeneous yet time-variable emissions originating from the periodically changing magnetospheric conditions can be separated from time-stationary emission inhomogeneities due to atmospheric anomalies.

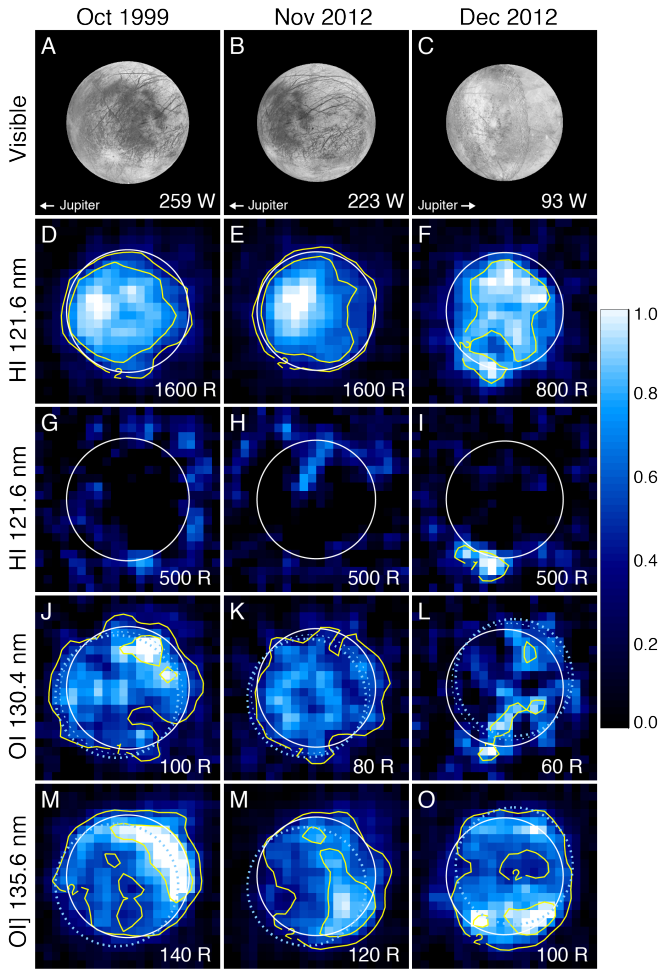

Fig. 1: Visible images of the observed hemispheres **(A-C)** with sub-observer longitudes listed and combined STIS images of the hydrogen and oxygen emissions **(D-O)** (Table 1). The Lyman-α morphology **(D-F)** reveals an anti-correlation with the brightness in the visible *(15)*. **(G-O)**: Same Lyman-α images, and OI130.4 nm and OI]135.6 nm images with solar disk-reflectance subtracted. 3×3 pixels are binned and the STIS images are smoothed to enhance visibility of the significant features. The dotted light blue circles indicate the multiplet lines *(15)*. The color scale is normalized to the respective brightness and the scale maximum (corresponding to 1.0 on the

scale) is listed in each image. Oversaturated pixels with intensities above maximum are white. The contours show signal-to-noise (SNR) ratios of the binned pixels (and contours for SNR=1 are omitted here in **(D-F**) and **(M-O**)).

After correction of the images for instrumental and background noise *(15)*, the remaining emission sources are: solar reflectance from Europa's surface, solar resonance scattering by atmospheric H and O atoms (negligible for OI135.6 nm), and electron impact (dissociative) excitation of atmospheric species, such as O_2, O and H_2O. To subtract the light reflected from the surface, we generated model spectral images by convolving normalized inverted visible images with a solar UV spectrum *(15)*. Whereas the surface reflectance corrected Lyman-α brightness is mostly consistent with a zero signal for the 1999 and November 2012 observations, a pronounced 400-600 R *(16)* region is found above the limb near the south pole in the residual Lyman-α emission in the December 2012 image (Fig. 1I).

The residual atmospheric oxygen emissions at 130.4 nm and 135.6 nm in contrast cover most of Europa's disk (Fig. 1J-O). The 135.6/130.4 ratios of 1.6±0.1 (both 1999 and November 2012) and 2.1±0.2 (December 2012) are consistent with previous measurements and an O_2 atmosphere with a low mixing ratio of O *(10,11)*. The oxygen aurora morphologies undergo considerable variations during the ~7 hours of all observations (Figs. 2,S1,S2). Bright OI]135.6 nm patches are found close to the poles, which appear to rock towards and away from Jupiter in correlation with the varying magnetic field orientation at Europa. The OI130.4 nm aurora pattern roughly resembles the OI]135.6 nm pattern (cf. I and N in Figs. S1 and S2, respectively) as expected if both OI multiplets originate from electron-impact dissociated O_2. Apparent deviations of the OI130.4 nm morphology from the OI]135.6 emission can be attributed in part to the inhomogeneity of the higher surface reflectance at 130.4 nm. This becomes most apparent in the combined images (Fig. 1J-L), because the time-variable atmospheric contributions are smoothed through the superposition. The generally patchy OI130.4 nm morphology is additionally affected by the low signal-to-noise ratio of the 130.4 nm emission *(15)*.

We focus our analysis on the emission above the limb of Europa, which is only marginally influenced by the surface reflectance due to instrument-scattered light from the on-disk features. Above the south polar limb in the December 2012 composite images an OI130.4 nm enhancement of similar appearance is found in the same region as the Lyman-α enhancement (compare Fig. 1I and L). Detectable Lyman-α and OI130.4 nm emissions are persistently found above the southern anti-Jovian limb during all five HST orbits of the December 2012 observations (Fig. 2A-J). Bright OI]135.6 nm emissions across the entire south polar region shift from the sub-Jovian to the anti-Jovian hemisphere between the first and last orbit (Fig. 2K-O). A persistent or significant above-limb OI]135.6 nm emission surplus is not detected.

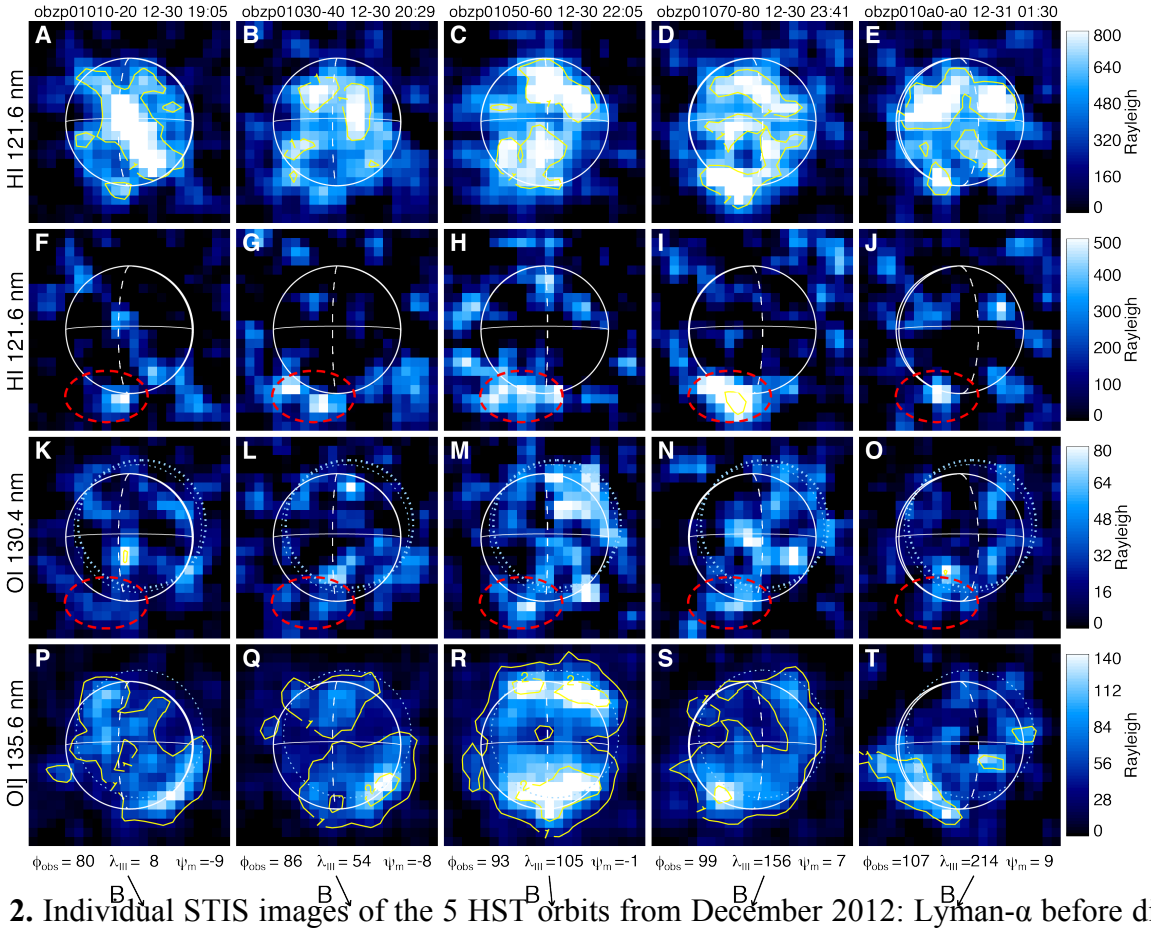

Fig. 2. Individual STIS images of the 5 HST orbits from December 2012: Lyman-α before disk-reflectance subtraction **(A-E)**, and reflectance-subtracted Lyman-α and oxygen emissions **(F-T).** The persistent plume emission is highlighted in dashed-red. Sub-observer longitude φ_{obs}, Jovian System-III-longitude λ_{III}, magnetic latitude ψ_{mag} and projected magnetic field line B are listed below. Leading meridian (90º W) is dashed-white, equator is solid-white. Other details are as in Fig. 1.

In a next step, we subdivided the region between 1 RE (Europa radius, 1561 km) and 1.25 RE (corresponding to an above-limb altitude of 390 km) in 18 bins spanning angles of 20º around the disk of Europa in all images (Fig. 3). The December 2012 Lyman-α image brightnesses of all pixels in limb bins #12 and #13 are 420±136 R and 604±140 R, which exceed the faint average limb emission of 46 R (outside the anomaly) by 2.8 and 4.0 times the propagated uncertainty (σ), respectively. The OI130.4 emission of 59±18 R in bin #13 is also significantly (2.4σ) higher than the average limb emission of 16 R, and bin #12 shows a slight enhancement (35±17 R). At both lines the emission anomaly appears to have two individual peaks in bins #12 and #13, which can, however, not be clearly separated within the measurement uncertainties. No significant emission

surplus is found in either of the bins at 135.6 nm (Fig. 3E). In 1999 and November 2012 all of the Lyman-α bins are consistent with zero signal within 2σ *(17)*.

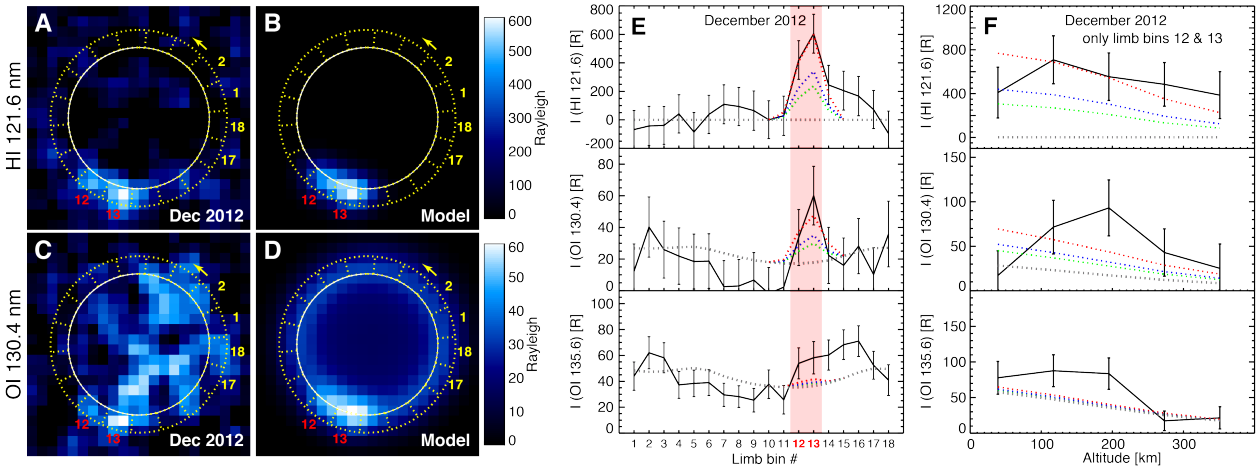

Fig. 3. Comparison of December 2012 observations and atmosphere plume model results: **(A-D)** Lyman-α and OI 130.4 nm STIS images (as in Fig. 1) and model aurora images from a global atmosphere with two H_2O plumes. The south polar above-limb emission is found in bins #12 and #13 of the eighteen 20º bins illustrated by the dotted yellow lines. The patchiness of the 130.4 nm on-disk emissions might originate from surface reflectance, atmospheric, or plasma inhomogeneities, but is also consistent with statistically expected variations across a uniform disk *(15)*. **(E)** Measured (solid black) and modeled (dotted) brightnesses of each 20º-wide limb bin around Europa's disk. The best-fit plume model atmosphere is shown in red, and plume densities decreased by factor 2 and factor 3 are shown in blue and green, respectively. **(F)** Radial profiles of measured and modeled brightness versus altitude in bins 12+13.

Detectable Lyman-α emission is not expected for the generally assumed abundance of hydrogen bearing molecules ($\leq 10^{17}$ m^{-2}) in the global sputtered atmosphere *(7-9)*. Lyman-α emission from a global atomic hydrogen corona that is not gravitationally bound as observed at Ganymede *(18)* would be isotropic. Lyman-α solar resonant scattering on atomic H also would require optically-thick columns ($> 10^{17}$ m^{-2}) to produce brightnesses >400 R and can be excluded. In contrast, H_2O freezes *(19)* and any enhancement must be localized to its source. In addition, electron impact on H_2O yields HI121.6 nm and OI130.4 nm, but has a lower cross section at 135.6 nm *(20)*. Hence, the emission surplus at HI121.6 nm and OI130.4 nm in an area, where no remarkable enhancement of OI]135.6 nm is found, suggests a local atmospheric H_2O enhancement.

We derive average H_2O and O_2 column densities using measured cross sections for electron-impact dissociative excitation and the standard plasma parameters for Europa *(15)*. Neglecting presumably small contributions from e+O or e+H_2O, the observed OI]135.6 nm brightness of bin #13 requires a line-of-sight O_2 column of $\sim 5 \times 10^{19}$ m^{-2}. The Lyman-α brightness in bin #13 implies an optically thin H_2O column density of 1.5×10^{20} m^{-2}. In this case, excitation of O_2 and H_2O would contribute 27 R and 29 R, respectively, to the OI130.4 nm emission consistent with the measured brightness of 59±18 R in bin #13. Thus, the Lyman-α/OI130.4 nm/OI]135.6 nm ratios are diagnostic of e + H_2O in an approach similar to the average OI]135.6 nm/OI130.4 nm ratio being diagnostic of e + O_2 *(10,11)*.

We generated model images for two three-dimensional plume distributions taking into account H_2O continuum absorption and resonant scattering. We started by generating a standard model for an average background atmosphere by adjusting the density of an exponentially decreasing O_2 atmosphere with low O and H_2O mixing ratios *(15)* to the observed OI]135.6 nm limb brightness for all observations (Fig. 3E,F, dotted grey). The fitted vertical O_2 column density of $N_{O2} = 3.5 \times 10^{18}$ m^{-2} agrees well with the observed OI130.4 limb brightness and is consistent with previous results *(7-11,21)*. Deviations from the model in several bins for both oxygen aurora lines are likely attributed to the variable plasma environment.

We then generated model images with two local H_2O plumes *(15)*. We adjusted the plume height of 200 km and the latitudinal expansion of 10º (or ~270 km on the surface) to the observed spatial profile of the Lyman-α emissions. The implemented density profile resembles an intermediate case between Io's shock-dominated Pele-type plumes *(22)* and the low-gravity outgassing of the Enceladus plumes *(23)*. Because the surface source locations cannot be determined from the images, the plumes were arbitrarily centered on the anti-Jovian meridian (180ºW) and in the center of the bins #12 and #13 at 55ºS and 75ºS, respectively. The densities of the plumes were fit to the observed Lyman-α bin brightness yielding total contents of 4.9×10^{31} and 8.2×10^{31} H_2O molecules for the plumes at 55ºS and 75ºS, respectively. The combined plume content is 1-2 orders of magnitude higher than the H_2O abundance in global atmosphere models without plumes *(7-9)*. The derived H_2O plume densities independently match the observed OI130.4 nm emission surplus if resonant scattering and electron impact on O with an estimated mixing ratio of $O/H_2O \sim 0.2\%$ is taken into account *(15)*.

The model reasonably reproduces the Lyman-α plume morphology and brightness decrease with altitude (Fig. 3). At low altitudes (< 100 km) the measured brightness decreases for both the Lyman-α and OI130.4 nm emission. Because bright OI]135.6 nm emission is also detected up to altitudes of 200 km, the OI130.4 nm profile might be best explained by a peak in oxygen abundance at higher altitudes. Also, the derived plume height of 200 km is higher than expected from model results *(24)* and would require large super-sonic eruption velocities of ~700 m/s. However, interpretation of the derived height and radial profile requires caution because of the systematic uncertainties of the disk location by 1-2 pixels or ~100 km. Moreover, a local density enhancement within a smooth global atmosphere would substantially alter the plasma environment, which in turn modifies the aurora morphology and brightness *(25)*.

The high plume velocities and relatively low number densities we inferred are consistent with vapor emission from narrow fractures *(15)*, as occurs at Enceladus *(23,26)*. The surface area of Europa's fractures is too small to produce a thermal anomaly detectable by the Galileo Photopolarimeter-Radiometer instrument *(27)*. Plume fallback could produce terrain softening in the near-polar regions, which might be detectable in suitable high-resolution images *(15)*.

The modeled Lyman-α limb brightnesses for the 1999 and November 2012 geometries are not consistent with persistent plumes. Also, no striking surplus of OI130.4 nm emission is detected. The model indicates that the plumes were less dense by at least a factor of 2 and 3 during the 1999 and November 2012 observations, respectively, if present (Fig. S3). Thus, the plume activity appears to undergo considerable variability.

Recently, the plumes at Enceladus' south pole have been shown to be more active near apocenter than at the pericenter *(28)*. Similar tidal stress variability for Europa is expected to open and close its Linea features (Fig. S4, *(15)*). Europa was very close to its apocenter during the December 2012 observations, and was shortly before and at the pericenter during the 1999 and November 2012 observations (Table 1). This causal relationship might explain the observed variability and the lack of detections in 1999 and November 2012. The plume variability, if real, verifies a key prediction of tidal-flexing models based on the existence of a subsurface ocean.

References and Notes:

1 M. H. Carr, *et al.*, Evidence for a subsurface ocean on Europa, *Nature*, **391**, 363 (1998);
2 R. T. Pappalardo, *et al.*, Does Europa have a subsurface ocean? Evaluation of the geological evidence, *J. Geophys. Res.*, **104** (1999);
3 K. K. Khurana, *et al.*, Induced magnetic fields as evidence for subsurface oceans in Europa and Callisto, *Nature*, **395**, 777-780 (1998);
4 B. E. Schmidt, D. D. Blankenship, G. W. Patterson, P. M. Schenk, Active formation of 'chaos terrain' over shallow subsurface water on Europa, *Nature*, **479**, 502-505 (2011);
5 C. B. Phillips, *et al.*, The search for current geologic activity on Europa, *J. Geophys. Res.*, **105** (2000);
6 S. A. Fagents, Considerations for effusive cryovolcanism on Europa: The post-Galileo perspective, *J. Geophys. Res.*, **108** (2003);
7 V. I. Shematovich, R. E. Johnson, J. F. Cooper, M. C. Wong, Surface-bounded atmosphere of Europa, *Icarus*, **173**, 480-498 (2005);
8 W. H. Smyth, M. L. Marconi, Europa's atmosphere, gas tori, and magnetospheric implications, *Icarus*, **181**, 510-526 (2006);
9 C. Plainaki, A. Milillo, A. Mura, S. Orsini, S. Massetti, T. Cassidy, The role of sputtering and radiolysis in the generation of Europa exosphere, *Icarus*, **218**, 956-966 (2012);
10 D.T. Hall, D. F. Strobel, P. D. Feldman, M. A. McGrath, H. A. Weaver, Detection of an oxygen atmosphere on Jupiter's moon Europa, *Nature*, ***373***, 677-679 (1995);
11 D. T. Hall, P. D. Feldman, M. A. McGrath, D. F. Strobel, The far-ultraviolet oxygen airglow of Europa and Ganymede, *Astrophys. J.*, ***499***(5), 475-481 (1998);
12 M. A. McGrath, C. J. Hansen, A. R. Hendrix, in *Europa*, R. T. Pappalardo, W. B. McKinnon, and K. K. Khurana (Univ. of Arizona Press, 2009), pp. 485-505;
13 T. A. Cassidy, R. E. Johnson, M. A. McGrath, M. C. Wong, J. F. Cooper, The spatial morphology of Europa's near-surface O_2 atmosphere, *Icarus*, **191**, 755-764 (2007);
14 J. Saur, *et al.*, Hubble Space Telescope/Advanced Camera for Surveys Observations of Europa's Atmospheric Ultraviolet Emission at Eastern Elongation, *Astrophys. J.*, **738** (2011);
15 See Supplementary Material for more information;
16 Rayleigh [R] is the column emission rate of 10^{10} photons per square meter per column per second, 1 R = $10^{10}/4\pi$ photons m^{-2} sr^{-1} s^{-1}.
17 The 1999 Lyman-α image might hint a plume feature in the south polar region (Fig. 1G), but is not statistically significant and is therefore not considered further.

18 C. A. Barth, *et al.*, Galileo ultraviolet spectrometer observations of atomic hydrogen in the atmosphere at Ganymede, *Geophys. Res. Lett.*, **24** (1997);
19 J. R. Spencer, L. K. Tamppari, T. Z. Martin, L. D. Travis, Temperatures on Europa from Galileo Photopolarimeter-Radiometer: Nighttime Thermal Anomalies, *Science*, **284** (1999);
20 O. P. Makarov, *et al.*, Kinetic energy distributions and line profile measurements of dissociation products of water upon electron impact, *J. Geophys. Res.*, **109(A18)** (2004);
21 J. Saur, D. F. Strobel, F. M. Neubauer, Interaction of the Jovian magnetosphere with Europa: Constraints on the neutral atmosphere, *J. Geophys. Res.*, **103(E9)** (1998);
22 J. Zhang, *et al.*, Simulation of gas dynamics and radiation in volcanic plumes on Io, *Icarus*, **163**, 182-197 (2003);
23 F. Tian, A. I. F. Stewart, O. B. Toon, K. W. Larsen, L. W. Esposito, Monte Carlo simulations of the water vapor plumes on Enceladus, *Icarus*, **188**, 154-161 (2007);
24 S. A. Fagents, *et al.*, Cryomagmatic Mechanisms for the Formation of Rhadamanthys Linea, Triple Band Margins, and Other Low-Albedo Features on Europa, *Icarus*, **144**, 54-88 (2000);
25 L. Roth, J. Saur, K. D. Retherford, D. F. Strobel, J. R. Spencer, Simulation of Io's auroral emission: Constraints on the atmosphere in eclipse, *Icarus*, **214**, 495-509 (2011);
26 C. J. Hansen, *et al.*, The composition and structure of the Enceladus plume. *Geophys. Res. Lett.*, ***38*(11)** (2011);
27 J. A. Rathbun, N. J. Rodriguez, J. R. Spencer, Galileo PPR observations of Europa: Hotspot detection limits and surface thermal properties, *Icarus*, **210(2)**, 763-769 (2010);
28 M. M. Hedman, *et al.*, An observed correlation between plume activity and tidal stresses on Enceladus, *Nature*, **500**, 182-184 (2013);

References continued (only called out in the SM)

29 Z. A. Selvans, "Time, tides and tectonics on icy satellites.", PhD thesis, University of Colorado at Boulder (2009);
30 F. Nimmo, J. R. Spencer, R. T. Pappalardo, M. E. Mullen, Shear heating as the origin of the plumes and heat flux on Enceladus. *Nature*, **447(7142)**, 289-291 (2007);
31 G. V. Hoppa, B. R. Tufts, R. Greenberg, P. E. Geissler, Strike-Slip Faults on Europa: Global Shear Patterns Driven by Tidal Stress, *Icarus*, **141**, 287-298 (1999);
32 G. V. Hoppa, R. Greenberg, B. R. Tufts, P. E. Geissler, Plume Detection on Europa: Locations of Favorable Tidal Stress, in *Lunar and Planetary Institute Science Conference Abstracts,* 30, p. 1603 (1999);
33 F. L. Roesler, *et al.*, Far-ultraviolet imaging spectroscopy of Io's atmosphere with HST/STIS, *Science*, **283**(5400), 353–357 (1999);
34 P. D. Feldman, *et al.*, HST/STIS Ultraviolet Imaging of Polar Aurora on Ganymede, *Astrophys. J.,* **535**, 1085–1090 (2000);
35 P. D. Feldman, *et al.*, Lyman-alpha Imaging of the SO_2 Distribution on Io, *Geophys. Res. Lett.*, **27**, 1787-1790 (2000);
36 K. D. Retherford, H. W. Moos, D. F. Strobel, B. C. Wolven, F. L. Roesler, Io's equatorial spots: Morphology of neutral UV emissions, *J. Geophys. Res.*, **105**, (2000);
37 K. D. Retherford, H. W. Moos, D. F. Strobel, Io's auroral limb glow: Hubble Space Telescope FUV observations, *J. Geophys. Res.*, **108**, 1333-1341 (2003);
38 B. C. Wolven, *et al.*, Emission profiles of neutral oxygen and sulfur in Io's exospheric corona, *J. Geophys. Res.*, **106(A11)**, 26155-26 (2001);

39 D. F. Strobel, J. Saur, J., P. D. Feldman, M. A. McGrath, Hubble Space Telescope space telescope imaging spectrograph search for an atmosphere on Callisto: A Jovian unipolar inductor. *Astrophy. J. Lett.*, **581(1)**, L51 (2002);
40 L. M. Feaga, M. A. McGrath, P. D. Feldman, The Abundance of Atomic Sulfur in the Atmosphere of Io, *Astrophys. J.*, **570**, 439-446 (2002);
41 L. M. Feaga, M. McGrath, P. D. Feldman, Io's dayside SO_2 atmosphere, *Icarus*, **201**, 570-584, (2009);
42 M. A. McGrath, *et al.*, Aurora on Ganymede, *J. Geophys. Res.*, **118**, 2043-2054 (2013);
43 L. Roth, J. Saur, K. D. Retherford, D. F. Strobel, P. D. Feldman, A phenomenological model for Io's UV aurora based on HST/STIS observations, *Icarus***, 228**, 386-406 (2014);
44 C. R. Proffitt, "Changes in the STIS FUVMAMA Dark Current", (Space Telescope STIS Instrument Science Report, Space Telescope Science Institute, 2007);
45 W. Curdt, *et al.*, The SUMER spectral atlas of solar-disk features, *Astronomy and Astrophysics*, **375**, 591-613 (2001);
46 T. N. Woods, *et al.*, Validation of the UARS solar ultraviolet irradiances: Comparison with the ATLAS 1 and 2 measurements, *J. Geophys. Res.*, 101(D6), 9541-9569 (1996);
47 T. N. Woods, *et al.*, Solar EUV Experiment (SEE): Mission overview and first results, *J. Geophys. Res.,* **110(A1)**, A01312 (2005);
48 J. E. Krist, R. N. Hook, F. Stoehr, 20 years of Hubble Space Telescope optical modeling using Tiny Tim, *Society of Photo-Optical Instrumentation Engineers (SPIE) Conference Series*, **8127** (2011);
49 R. Greeley, *et al.*, , Bagenal, F., T. E. Dowling and W.B. McKinnon (Cambridge Univ. Press, 2004), pp. 457-483;
50 R. L. Lucke, R. C. Henry, W. G. Fastie, Far-ultraviolet albedo of the moon, *Astronom. J.*, **81**, 1162-1169 (1976);
51 R. C. Henry, W. G Fastie, R. L. Lucke, B. Q. Hapke, B. W. A far-ultraviolet photometer for planetary surface analysis. *The moon*, **15(1-2)**, 51-65 (1976);
52 J. P. Doering, E. E. Gulcicek, Absolute differential and integral electron excitation cross sections for atomic oxygen. VII - The ^3P-^1D and ^3P-^1S transitions from 4.0 to 30 eV, *J. Geophys. Res.,* **94**, 1541–1546 (1989);
53 J. P. Doering, E. E. Gulcicek, Absolute differential and integral electron excitation cross sections for atomic oxygen. VIII - The ^3P-$^5S_0$ transition (1356 Å) from 13.9 to 30 eV, *J. Geophys. Res.*, **94**, 2733–2736 (1989);
54 J. P. Doering, Absolute differential and integral electron excitation cross sections for atomic oxygen. IX - Improved cross section for the ^3P-^1D transition from 4.0 to 30 eV. *J. Geophys. Res*., **97**, 19531–19534 (1992);
55 I. Kanik, *et al.*, Electron impact dissociative excitation of O_2: 2. Absolute emission cross sections of the OI(130.4 nm) and OI(135.6 nm) lines, *J. Geophys. Res.*, **108**, 5126 (2003);
56 P. V. Johnson, I. Kanik, D. E. Shemansky, X. Liu, Electron-impact cross sections of atomic oxygen. *J. of Physics B: Atomic, Molecular and Optical Physics*, **36(15)**, 3203 (2003);
57 S. P. Sander, *et al.*, "Chemical Kinetics and Photochemical Data for Use in Atmospheric Studies, Evaluation No. 17" (JPL Publication 10-6, Jet Propulsion Laboratory, Pasadena, 2011);
58 K. Yoshino, W.H. Parkinson, K. Ito, T. Matsui, Absolute absorption cross-section measurements of Schumann Runge continuum of O_2 at 90 and 295 K, *J. of Molecular Spectroscopy*, **229**, 238-243 (2005);

59 H.-C. Lu, K.-K. Chen, H.-F. Chen, B.-M. Cheng, J.F. Ogilvie, Absorption cross section of molecular oxygen in the transition E $^3\Sigma_u^-$ v = 0 – X $^3\Sigma_g^-$ v = 0 at 38 K, *Astronom. Astrophys.*, **520** (2010);
60 T. Harb, W. Kedzierski, J. W. McConkey, Production of ground state OH following electron impact on H_2O, *J. Chem. Phys.*, **115**, 5507-5512 (2001);
61 J. S. Lee, R. R. Meier, Angle-dependent frequency redistribution in a plane-parallel medium - External source case, *Astroph. J.*, **240**, 185-195 (1980);
62 D. C. Morton, Atomic data for resonance absorption lines. I - Wavelengths longward of the Lyman limit, *Astrophys. J. Suppl.*, **77**, 119-202 (1991);
63 J. Marti, K. Mauersberger, A survey and new measurements of ice vapor pressure at temperatures between 170 and 250K. *Geophys. Res. Lett.*, **20(5)**, 363-366 (1993);
64 J. D. Goguen, *et al.*, The temperature and width of an active fissure on Enceladus measured with Cassini VIMS during the 14 April 2012 South Pole flyover, *Icarus*, ***226*(1)**, 1128-1137 (2013);
65 P. Schenk, J. Schmidt, O. White. The Snows of Enceladus. In *EPSC-DPS Joint Meeting 2011*, Vol. 1, 1358 (2011);
66 A. P. Ingersoll, A. A. Pankine, Subsurface heat transfer on Enceladus: Conditions under which melting occurs. *Icarus*, **206(2)**, 594-607 (2010);
67 F. Nimmo, Stresses generated in cooling viscoelastic ice shells: Application to Europa, *J. Geophys. Res.,* **109(E12)** (2004);
68 H. Hussmann, T. Spohn, Thermal-orbital evolution of Io and Europa. *Icarus*, **171(2)**, 391-410 (2004);
69 A. P. Ingersoll, S. P. Ewald, Total particulate mass in Enceladus plumes and mass of Saturn's E ring inferred from Cassini ISS images. *Icarus*, **216(2)**, 492-506 (2011);
70 F. Nimmo, P. D. Thomas, R. T. Pappalardo, W. B. Moore, The global shape of Europa: Constraints on lateral shell thickness variations. *Icarus*, **191(1)**, 183-192 (2007);

Acknowledgments: This work is based upon Hubble Space Telescope observations available at the NASA MAST data archive. Support for program number GO-13040 was provided by NASA through a grant from the Space Telescope Science Institute, which is operated by the Association of Universities for Research in Astronomy, Inc., under contract NAS5-26555; and by Verbundforschung Astronomie und Astrophysik.

Table 1. HST/STIS G140L observations of Europa's UV emissions ([a:] PI McGrath, [b:] PI Saur)

Observation start date and time	HST orbits/ ex-posures	Total exp. time [min]	Spatial resolution [km/pixel]	Sub-observer W long. [º]	System III longitude [º]	Mag. lat. range [º]	True anomaly f [º]	Water vapor detected
5-Oct-1999 8:39 [a]	5 / 9	156	71.5	245 – 274	300 – 158	-9.5 – 6.8	343 – 13	No
8-Nov-2012 20:41 [b]	5 / 10	183	73.9	209 – 238	25 - 243	-9.3 – 9.5	289 - 318	No
30-Dec-2012 18:49 [b]	5 / 9	164	74.9	79 – 108	0 – 218	-9.5 – 9.5	185 - 218	Yes